ADVANCED MATERIALS
www.advmat.de

Check for updates

Strain-Engineered Metal-to-Insulator Transition and Orbital Polarization in Nickelate Superlattices Integrated on Silicon

*Binbin Chen, Nicolas Gauquelin, Daen Jannis, Daniel M. Cunha, Ufuk Halisdemir, Cinthia Piamonteze, Jin Hong Lee, Jamal Belhadi, Felix Eltes, Stefan Abel, Zoran Jovanović, Matjaž Spreitzer, Jean Fompeyrine, Johan Verbeeck, Manuel Bibes, Mark Huijben, Guus Rijnders, and Gertjan Koster**

Epitaxial growth of $SrTiO_3$ (STO) on silicon greatly accelerates the monolithic integration of multifunctional oxides into the mainstream semiconductor electronics. However, oxide superlattices (SLs), the birthplace of many exciting discoveries, remain largely unexplored on silicon. In this work, $LaNiO_3/LaFeO_3$ SLs are synthesized on STO-buffered silicon (Si/STO) and STO single-crystal substrates, and their electronic properties are compared using dc transport and X-ray absorption spectroscopy. Both sets of SLs show a similar thickness-driven metal-to-insulator transition, albeit with resistivity and transition temperature modified by the different amounts of strain. In particular, the large tensile strain promotes a pronounced Ni $3d_{x^2-y^2}$ orbital polarization for the SL grown on Si/STO, comparable to that reported for $LaNiO_3$ SL epitaxially strained to $DyScO_3$ substrate. Those results illustrate the ability to integrate oxide SLs on silicon with structure and property approaching their counterparts grown on STO single crystal, and also open up new prospects of strain engineering in functional oxides based on the Si platform.

Successful epitaxy of $SrTiO_3$ (STO) directly on silicon using molecular beam epitaxy represents a milestone toward the monolithic integration of multifunctional oxides into the mainstream semiconductor electronics.[1] However, oxide superlattices (SLs) remain scarcely explored on silicon, hindered by the difficulties in growing oxide layers on silicon with a 2D mode. Over the past two decades, forming SLs has been demonstrated to be a powerful tool to engineer oxide functionalities as well as to explore novel electronic states by manipulating the dimensionality, interfacial, and/or interlayer interactions.[2–4] $LaNiO_3$ (LNO)-based SLs have aroused enormous interest due to the possibility of creating a cuprate-like Fermi surface through heterostructuring.[5,6] Bulk LNO is a paramagnetic metal lacking any long-range ordering phenomena at all

Dr. B. Chen, D. M. Cunha, Dr. U. Halisdemir, Prof. M. Huijben, Prof. G. Rijnders, Prof. G. Koster
MESA+ Institute for Nanotechnology
University of Twente
Enschede 7500 AE, The Netherlands
E-mail: g.koster@utwente.nl

Dr. N. Gauquelin, D. Jannis, Prof. J. Verbeeck
Electron Microscopy for Materials Science (EMAT)
University of Antwerp
Antwerp 2020, Belgium

Dr. C. Piamonteze
Swiss Light Source
Paul Scherrer Institut
Villigen PSI
Villigen CH-5232, Switzerland

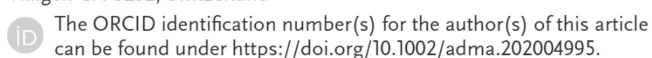
The ORCID identification number(s) for the author(s) of this article can be found under https://doi.org/10.1002/adma.202004995.

© 2020 The Authors. Advanced Materials published by Wiley-VCH GmbH. This is an open access article under the terms of the Creative Commons Attribution License, which permits use, distribution and reproduction in any medium, provided the original work is properly cited.

DOI: 10.1002/adma.202004995

Dr. J. H. Lee, Dr. M. Bibes
Unité Mixte de Physique
CNRS
Thales
Université Paris-Saclay
Palaiseau 91767, France

Dr. J. Belhadi, Dr. Z. Jovanović, Prof. M. Spreitzer
Advanced Materials Department
Jožef Stefan Institute
Ljubljana 1000, Slovenia

Dr. F. Eltes, Dr. S. Abel, Dr. J. Fompeyrine
IBM Research Europe
Rüschlikon, Zürich 8803, Switzerland

Dr. F. Eltes, Dr. S. Abel, Dr. J. Fompeyrine
Lumiphase AG
Zürich 8003, Switzerland

Dr. Z. Jovanović
Laboratory of Physics
Vinča Institute of Nuclear Sciences
University of Belgrade
Belgrade 11000, Serbia

 © 2020 The Authors. Advanced Materials published by Wiley-VCH GmbH

temperatures. The nominal Ni^{3+} ion has a $3d^7$ configuration with filled t_{2g} orbitals and one electron residing in the doubly degenerate e_g orbitals. To remove the degeneracy and obtain a single band Fermi surface with only x^2-y^2 character, two main strategies have been proposed, namely tensile epitaxial strain and quantum confinement.[7–11] Although lots of experimental efforts have been made by combining these two effects, the observed orbital polarization is much smaller than theoretically predicted.[9] This has been attributed to the strongly correlated nature of LNO. The on-site Hund interaction and negative charge transfer energy favor a high-spin Ni $3d^8\underline{L}$ ($\underline{L}$ represents an oxygen hole) state, which is not susceptible to orbital polarization.[12]

Aside from orbital control, the thickness-driven metal-to-insulator transition (MIT) is another long-standing issue in LNO thin films and the underlying mechanism has not been fully understood. Scherwitzl et al. reported a crossover from metallic to strongly localized behavior upon reducing the film thickness, while weak localization (WL) was observed in the intermediate thickness range. The results point to the importance of disorder in triggering the MIT.[13,14] In sharp contrast with the scenario of gradual localization of electrons, angle-resolved photoemission spectroscopy revealed a sudden breakdown of the Fermi liquid-like quasiparticles at a critical LNO thickness of 2 unit cells (uc).[15] This has been ascribed to the onset of a spin/charge ordered state in the quasi 2D LNO sheet, resembling the emergent antiferromagnetic order reported in $LNO/LaAlO_3$ (LAO) SL with the same LNO layer thickness.[3,16] Furthermore, the buckling of NiO_2 planes and removal of apical oxygen at the surface have also been invoked as being the driving forces for the insulating states in ultrathin LNO films.[17,18]

Strain effect has been extensively studied in LNO by growing epitaxial films on oxide substrates possessing different lattice constants.[10,11,19–21] In particular, for LNO films grown on Si, an additional thermal strain will come into play which arises from the large differences in thermal expansion coefficients (TECs) between LNO and Si.[22,23] Although LNO has been widely used as electrodes for ferroelectric capacitors integrated on Si,[24–26] the impact of thermal-strain on its properties has not yet been assessed. Here, we compared the strain states, thickness-driven MITs and orbital states in $LNO/LaFeO_3$ (LFO) SLs grown on STO single crystal and STO-buffered Si (Si/STO) substrates. The in-plane lattice parameter of the SL on Si/STO substrate decays with increasing the layer thickness of LNO, n in uc, but remains larger than the corresponding SL fully strained to STO. Upon reducing n, the SLs on both substrates gradually turn into a strongly localized state at $n = 3$. The larger strain on Si/STO leads to an enhanced MIT temperature (T_{MI}) at $n = 4$ as well as increased resistivity at $n = 1$, 2. The electron conduction mechanisms are hardly affected by the different amounts of strain in the entire thickness range. In particular, the strain promotes a prominent Ni $3d_{x^2-y^2}$ orbital polarization for the SL grown on Si/STO, as revealed by X-ray absorption spectroscopy (XAS). Such orbital polarization, however, is negligible in the corresponding SL grown on STO.

LNO/LFO SLs were fabricated on (001)-oriented STO and Si/STO substrates using pulsed laser deposition in situ monitored by reflection high-energy electron diffraction (RHEED). The STO buffer layer with thickness of 4 nm was prepared on Si using molecular beam epitaxy and the growth details can be found elsewhere.[27] The layer thickness of LNO was varied from $n = 1$ to 8 uc, while the LFO layer was set to 5 uc thick. The LNO/LFO bilayer was repeated ten times to form the SL. The spacer layer LFO is a charge-transfer insulator with a band gap of ≈2.2 eV.[28] The stable $3d^5$ electronic configuration of Fe^{3+} prohibits the interfacial charge transfer between LNO and LFO,[29] as confirmed by XAS measurements shown later in this paper. Regarding the crystal structure, LFO is orthorhombic with a pseudocubic lattice constant $a_0 = 3.93$ Å,[30] and LNO is rhombohedral with $a_0 = 3.838$ Å.[21] The LNO and LFO layers grow in a layer-by-layer mode on STO (Figure S1, Supporting Information), yielding a streaky RHEED pattern and a terraced surface for the $n = 1$ SL (**Figure 1**a). By contrast, the corresponding SL grown on Si/STO shows streaks with some intensity modulations, which are caused by the increasing electron transmission through surface grains.[31] Nevertheless, the surface remains smooth with a root-mean-square roughness of ≈2.8 Å (Figure 1b). The orthorhombic symmetry of the topmost LFO layer is manifested by the half-order streaks as indicated with white arrows in Figure 1a,b.[32]

Figure 1c,d shows the high-resolution X-ray diffraction (XRD) patterns of LNO/LFO SLs grown on STO and Si/STO, respectively. Two 20-uc thick LNO single films are included for reference. Clear Laue fringes can be appreciated for all the SLs on STO, attesting to their smooth surfaces. The presence of satellite peaks indicates a chemically modulated structure with well-defined interfaces between the component layers. The periodicity deduced from such satellite peaks agrees well with the designed value. For the SLs grown on Si/STO, they are (00l)-single oriented without forming secondary phases. Satellite peaks are observed only for SLs with $n \geq 3$, while Kiessig fringes are hardly visible for all SLs. The in-plane epitaxial relationship was ascertained by XRD φ scans (Figure S2a, Supporting Information), where the unit cell of oxide layers was rotated 45° with respect to Si. We also compared the crystallinity for SLs grown on STO and Si/STO by measuring XRD rocking curves around SL $(002)_{pc}$ peaks (Figure S2b,c, Supporting Information). The SLs on Si shows a typical full width at half-maximum of ≈0.50°, six times larger than that of the SLs on STO (≈0.08°). The deteriorated crystalline quality for the SLs on Si/STO can be related to the defects in STO buffer layer as well as to the thermal strain from Si substrate.[33] For both sets of SLs, as n decreases, the SL peaks gradually shift to lower angles because of the relatively smaller lattice constant of LNO as compared to LFO. The crystal structure at atomic level has been characterized using high-resolution scanning transmission electron microscopy (Figure S3, Supporting Information). The lattice coherence is maintained within the scanning area for both SLs grown on STO and Si/STO without forming dislocations.

The strain states of LNO single films and LNO/LFO SLs grown on STO and Si/STO are assessed based on XRD reciprocal space mappings (RSMs) as depicted in **Figure 2**a–g. The extracted in-plane and out-of-plane lattice constants a and c are plotted as a function of n in Figure 2h. As n increases, the reflections gradually shift to larger Q_Z values for SLs grown on both substrates, in accordance with the decline of the average c.

© 2020 The Authors. Advanced Materials published by Wiley-VCH GmbH

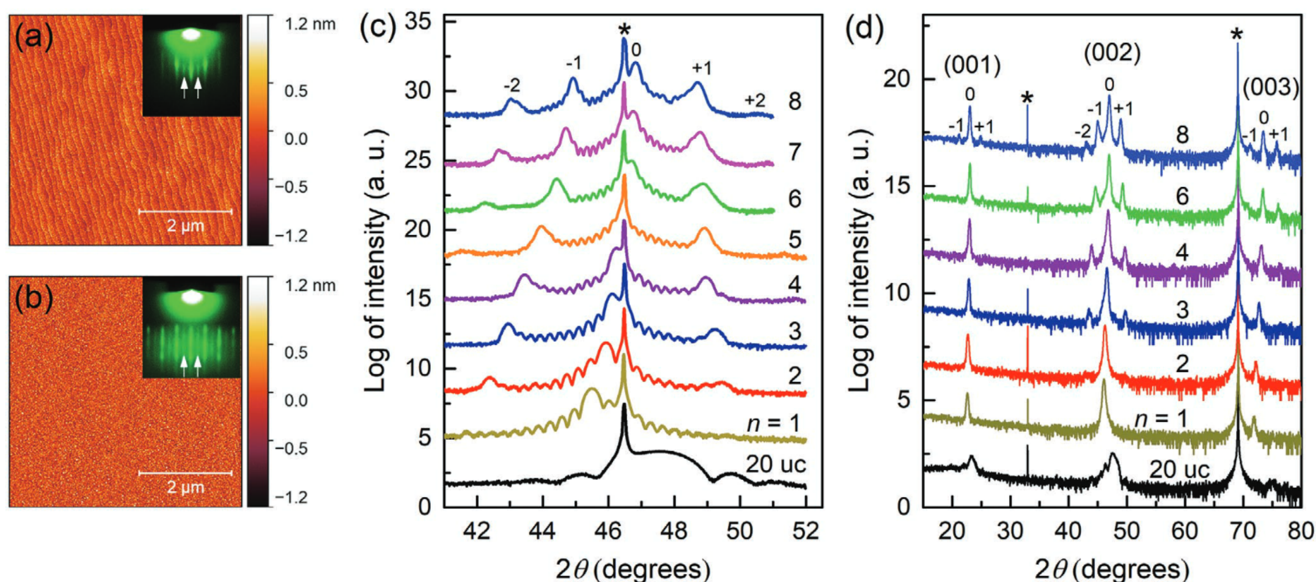

Figure 1. Characterization of LNO/LFO SLs grown on STO (001) and Si/STO (001) substrates. a,b) AFM images of the $n = 1$ SLs grown on STO (a) and Si/STO (b). The insets show RHEED patterns taken along STO [100] azimuth, with white arrows indicating the half-order streaks. c,d) High-resolution XRD θ–2θ scans of LNO/LFO SLs with varied n, grown on STO (c) and Si/STO (d) substrates. The substrate peaks of STO and Si are marked with asterisks and the superlattice peaks are indexed for the $n = 8$ SLs. Two 20-uc thick LNO single films are included for comparison.

The LNO single film and SLs on STO share the same Q_X value with the substrate, manifesting their coherently strained states. Thus a is derived as 3.905 Å and an in-plane tensile strain of ≈1.7% is applied to the LNO layer. By contrast, all the samples on Si/STO are relaxed from Si substrate. The reflections show a broad feature caused by the in-plane mosaicity.[34] As n increases, the SL reflection on Si/STO gradually shifts to larger Q_X values, corresponding to a decreasing a (Figure 2h). This can be understood by the thin nature of the 4 nm STO buffer layer, which is largely relaxed from Si at growth temperature (≈650 °C) and unlikely to fix the in-plane lattice of the relatively thick SL.[22,34] Therefore, a of LNO/LFO SL at 650 °C is determined by the thickness ratio of LNO and LFO, and decays with n given the smaller lattice constant of LNO compared to LFO. During cooling down to room temperature, the lattice of oxide SLs follows the shrinkage of the thick Si substrate, which

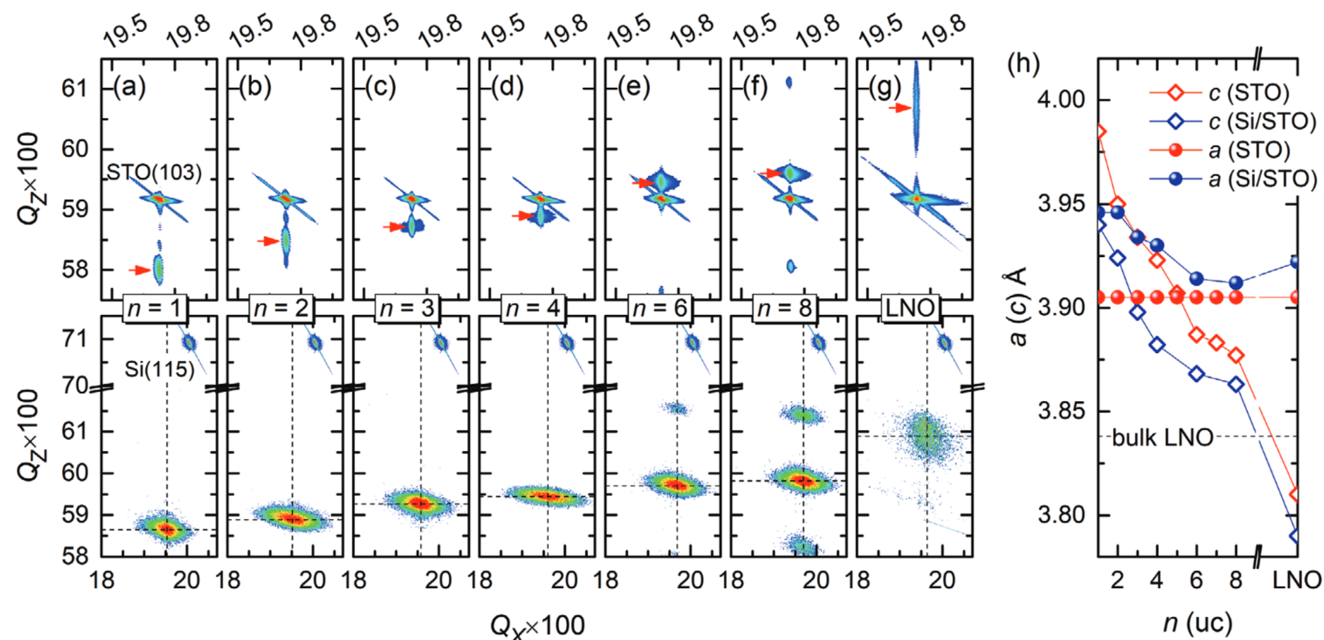

Figure 2. Strain contrast between LNO/LFO SLs grown on STO and Si/STO. a–g) RSMs of $(103)_{pc}$ reflection for SLs grown on STO (top panels) and Si/STO (bottom panels). The black dotted lines in the bottom panels mark Q_X and Q_Z positions of the SLs on Si/STO. h) Extracted a and c as a function of n.

© 2020 The Authors. Advanced Materials published by Wiley-VCH GmbH

has a drastically smaller TEC ≈2.6×10^{-6} °C^{-1} as compared to LFO (≈11.6×10^{-6} °C^{-1}) and LNO (≈10×10^{-6} °C^{-1}).[22,35,36] As a consequence, a thermal tension is usually introduced to the oxide films grown on Si. This thermal strain, however, is negligible for the SLs grown on STO substrates. Taken together, for LNO/LFO SLs grown on Si/STO, the strain state of LNO is dictated by the interfacial strain from neighboring LFO layers together with the tensile thermal strain from Si. The contribution of thermal strain is evident for the SLs with $n = 1$ and 2. They show roughly the same $a = 3.946$ Å, greater than the bulk value of LFO ($a_0 = 3.93$ Å). LNO single films show a sharp and elongated spot on STO, but a rather diffuse spot on Si/STO due to its relatively poor crystallinity (Figure S2c, Supporting Information). Note that the thermal strain yields $a \approx 3.922$ Å for LNO film grown on Si/STO, larger than the corresponding film on STO having $a = 3.905$ Å. To gain some clues about the strain accommodations in LNO, we estimate c of LNO single films based on a volume conserving scenario. Using $a_0 = 3.838$ Å and Poisson ratio $\nu = 0.27$,[37] we have $c = \frac{2\nu}{\nu-1}a - \frac{\nu+1}{\nu-1}a_0 = 3.788$ Å (3.776 Å) for the LNO film grown on STO (Si/STO), which is smaller than $c = 3.81$ Å (3.79 Å) measured from XRD. This hints the in-plane tensile strain is not simply accommodated by the contraction of NiO_6 octahedra along the out-of-plane direction. Notably, half-order Bragg diffractions reveal that NiO_6 octahedral rotations are suppressed along the out-of-plane direction to match the lattice of STO in tensile-strained LNO/STO film.[11,21] This is probably accompanied by an additional breathing distortion of NiO_6 octahedra as suggested by density functional calculations.[20] The strain accommodation in LNO plays a pivotal role in the Ni e_g orbital occupancy as we will show below.

The thickness-driven MITs in LNO/LFO SLs grown on STO and Si/STO are compared in **Figure 3**a,b. Here the resistances of the highly insulating LFO films grown on STO and Si/STO are outside the accessible measurement range, and the resistivity is calculated by only considering the contribution from LNO layers. The transport properties show the same tendency with decreasing n for SLs grown on the two different substrates. The SLs are metallic ($d\rho/dT > 0$) for $n > 6$ and turn insulating ($d\rho/dT < 0$) for $n < 4$, while temperature-driven MIT is observed at low temperature for $4 \le n \le 6$. As shown in Figure S4, Supporting Information, the sheet resistances of the $n = 3$ SLs cross the quantum of resistance in 2D, ≈25 kΩ, indicative of a crossover from weak to strong electron localization. It is interesting to note that LNO single films grown on STO becomes insulating at a larger critical thickness of 5 uc.[13] The reduced critical thickness in LNO/LFO SLs may benefit from the neighboring LFO layer, which maintains a bulk-like coordination environment (LaO–NiO_2–LaO) for the interfacial NiO_2 plane.[17] The room-temperature resistivity, $\rho_{(300\ K)}$ is plotted as a function of n in **Figure 4**a. The SLs grown on STO and Si/STO show only slight differences in $\rho_{(300\ K)}$ when $n \ge 3$, although the SLs on Si/STO show a degraded crystallinity. However, the insulating SLs ($n \le 2$) on Si/STO show a substantially larger $\rho_{(300\ K)}$ than the ones on STO. Note that the $n = 1$ SL on Si/STO is too resistive to be measured. This can be linked to the reduced dimension as well as the large amount of strain (≈2.8%) on Si substrate, both of which narrow Ni-3d bandwidth.[19] Regarding T_{MI} depicted in the inset of Figure 4a, the $n = 6$ SLs show essentially the same T_{MI} of ≈41 K on both substrates because of the small difference in strain. However, T_{MI} is enhanced by strain from 156 K on STO to 207 K on Si/STO for the $n = 4$ SL.

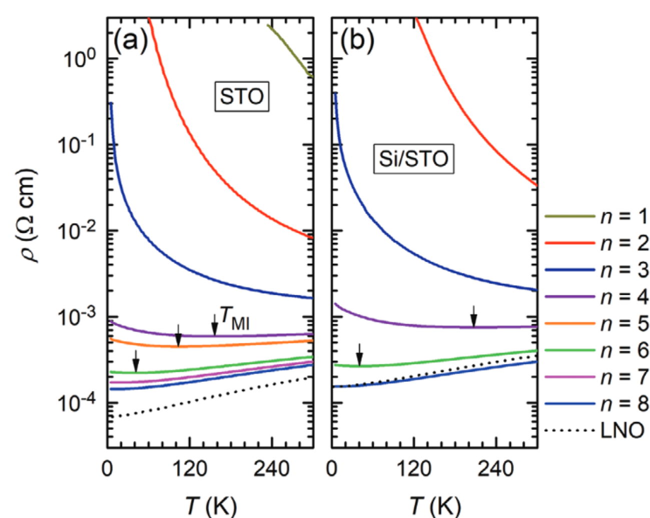

Figure 3. Thickness-driven MITs in LNO/LFO SLs. a,b) ρ–T curves of LNO/LFO SLs with varied n grown on STO (a) and Si/STO (b) substrates. The resistivity is normalized to the total thickness of LNO. The arrows mark the onset temperature of resistivity upturn, T_{MI}.

To gain further insights into the conduction mechanisms, the transport behaviors are fitted to appropriate models as shown in Figure 4b–d. The ρ–T curves of metallic LNO films and $n = 8$ SLs are fitted with $\rho = \rho_0 + AT^{\alpha}$, where ρ_0 is the residual resistivity and α is determined by the dominant electron scattering process. According to Fermi liquid theory, the dominant electron–phonon (electron–electron) scattering at high (low) temperature yields $\alpha = 1$ ($\alpha = 2$).[38] Surprisingly, the four samples can be well fitted with $\alpha = 1.5 \pm 0.05$ in a wide temperature range (40–300 K). Such a $T^{3/2}$ power law is different from the sputtered LNO/STO film showing a typical Fermi liquid behavior with a T^2 dependence.[13] We notice that this $T^{3/2}$ scaling has also been observed in LNO/STO films fabricated by molecular beam epitaxy, as well as in LNO/LAO SLs.[39–41] The deviation from the conventional Fermi liquid behavior is ascribed to the presence of bond-length fluctuations when the system is on the verge of MIT.[42] For the $n = 6$ SLs, the resistivity upturn at low temperature is well described by the WL model, where the self-interference of electron waves around disorders enhances backscattering and thus increases the resistivity.[13] In 2D systems,

$$\sigma = \sigma_0 + p\frac{e^2}{\pi h}\ln\left(\frac{T}{T^*}\right) \tag{1}$$

where σ_0 is the Drude conductivity and T^* is related to the mean free path for electron hopping. p is determined by the main inelastic scattering process, that is, the dominant electron–electron collision and electron–phonon scattering give $p = 1$ and $p = 3$, respectively.[13] As can be seen from Figure 4c, the SLs grown on STO and Si/STO are fitted with slopes of 1.3×10^{-5} S and 1.38×10^{-5}, corresponding to $p \approx 1$. Therefore, the electron–electron collision dominates at low temperature, in line with previous

© 2020 The Authors. Advanced Materials published by Wiley-VCH GmbH

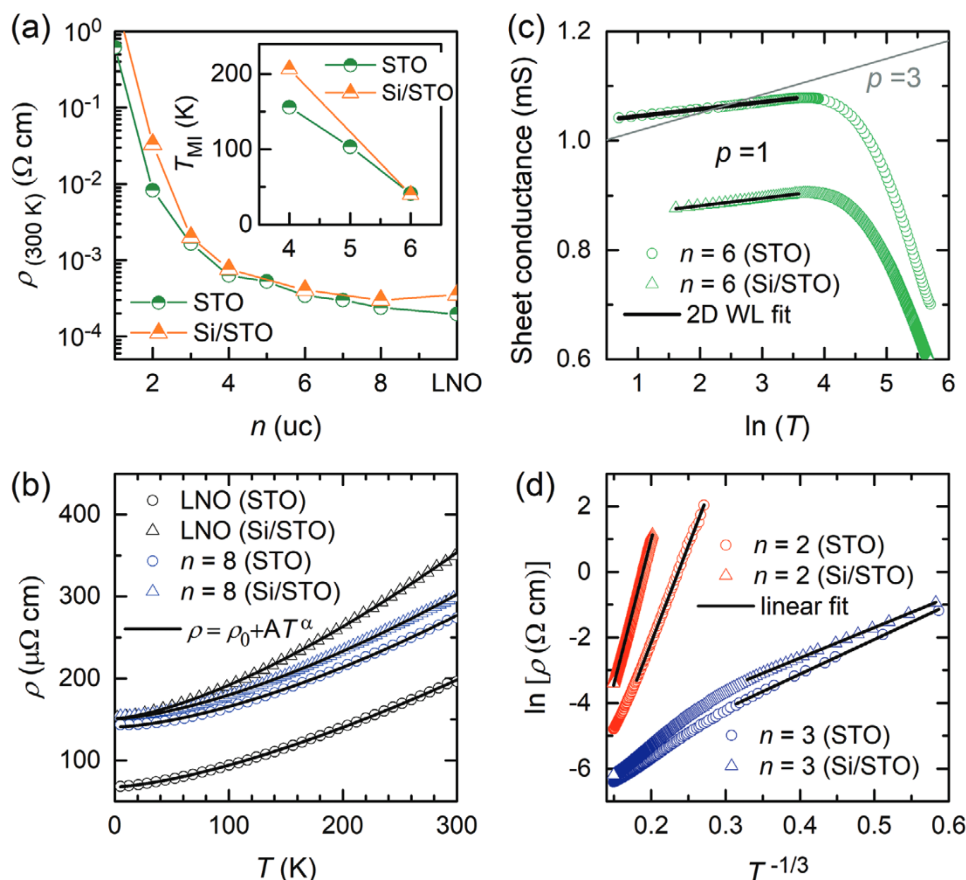

Figure 4. Modeling conduction mechanisms in LNO/LFO SLs. a) Room-temperature resistivity $\rho_{(300\ K)}$ and T_{MI} (inset) as a function of n. b) ρ–T curves of the metallic LNO single films and $n = 8$ SLs grown on STO and Si/STO. The solid lines are fits to $\rho = \rho_0 + AT^{\alpha}$. c) Sheet conductance plotted against $\ln(T)$ for the $n = 6$ SLs, with fittings to the 2D WL model. The sheet conductance is calculated for the LNO individual layer considering a parallel resistor model. The fittings give $p \approx 1$ for both samples, and the case of $p \approx 3$ is shown by the gray line. d) Logarithm of resistivity as a function of $T^{-1/3}$ for the SLs with $n = 2$ and 3, with fittings to the 2D VRH model.

studies on LNO/STO single films and LNO/LAO SLs.[13,40] The WL model is further supported by the presence of negative magnetoresistance (Figure S5, Supporting Information). Interestingly, a butterfly-like feature was observed at 2 K, signifying an emergent magnetism in the system. This is beyond the scope of this paper and deserves further investigation. The insulating SLs with n = 2 and 3 (Figure 4d) are fitted to the 2D variable-range hopping (VRH) model given by $\rho = \rho_0 \exp[(T_0/T)^{1/3}]$. Here T_0 can be written as $T_0 = 13.8/[k_B N(E_F)\xi^2]$, with $N(E_F)$ and ξ being the density of states near Fermi level and the electron localization length. Upon reducing LNO layer thickness from 3 to 2 uc, T_0 rapidly increases from 1187 K (803 K) to 2.06×10^5 K (6.81×10^5 K) for the SLs grown on STO (Si/STO), indicating that electrons become much more localized due to the increasing disorders. Note that the mean hopping energy estimated by $E_0 = 1/3 k_B T^{2/3} T_0^{1/3}$ is larger than $k_B T$ in the fitting temperature range, validating the use of a 2D-VRH model.[40] Altogether, LNO/LFO SLs gradually evolve from a metallic to a strongly localized state as n decreases. The electron conduction mechanism in LNO is hardly altered by the strain on Si substrate.

To study the effects of the different amounts of strain on the charge and orbital states, we performed XAS measurements on the n = 4 SLs grown on STO and Si/STO as shown in **Figure 5**. The polarization averaged XAS spectra around Ni and Fe L edges were collected with a bulk sensitive fluorescence yield mode (Figure 5a). By comparison to the reference spectra of Fe_2O_3 and bulk LNO,[11,43] we can confirm the stable Fe^{3+} and Ni^{3+} states, and exclude the presence of substantial oxygen vacancies and electron transfer across the interface. In order to probe the orbital states of Ni^{3+} e_g electrons, we measured the XAS spectra using σ and π linearly polarized photons. Given the overlap between La M_4 and Ni L_3 edges, we focus on the Ni L_2 edge as shown in Figure 5b,c. The linear dichroism is derived as $I(ab) - I(c)$, with $I(ab)$ and $I(c)$ being the in-plane and out-of-plane polarized XAS absorptions, respectively. Here $I(ab) = I(\sigma)$ and $I(c) = [I(\pi) - I(ab)\sin^2\theta]/\cos^2\theta$, where θ is the angle between the incoming X-ray and sample plane and set at 30° in our experiments. For the SL grown on STO, the spectra are essentially the same for σ and π polarizations and negligible X-ray linear dichroism signal is observed, suggestive of a degenerated e_g state as sketched in the inset of Figure 5b. By contrast, for the SL on Si/STO, the σ-polarized spectrum shows a reduced intensity and shift to lower energy with respect to the π-polarized spectrum. This means that the in-plane x^2–y^2 orbital has a lower energy and higher electron occupancy than the $3z^2$–r^2 orbital.[44] We also measured the spectra with the surface

© 2020 The Authors. Advanced Materials published by Wiley-VCH GmbH

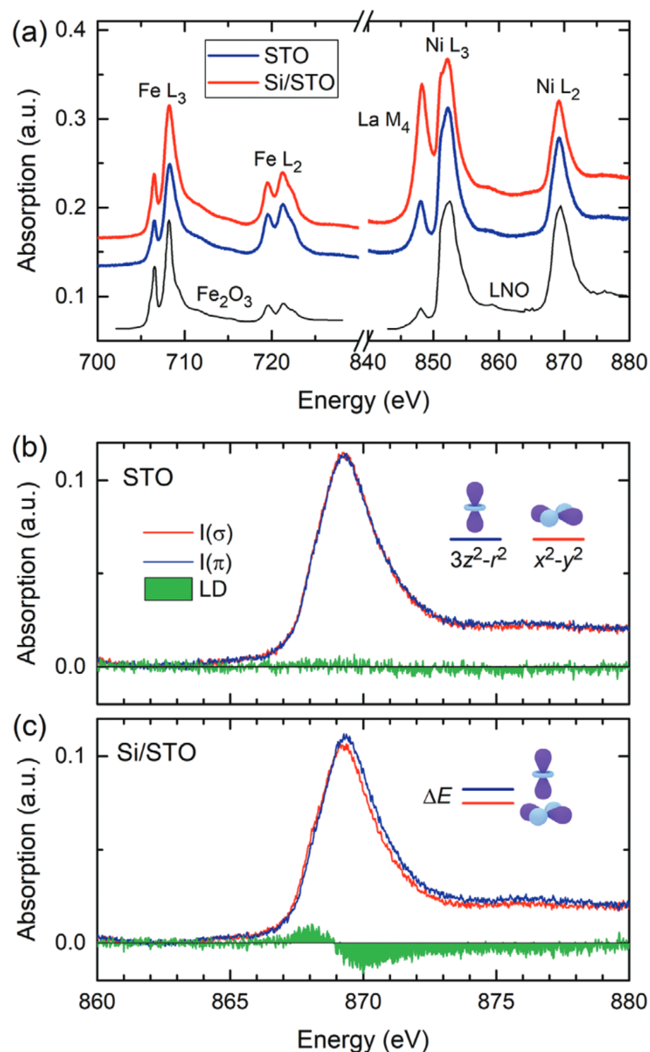

Figure 5. Charge and orbital states in the $n = 4$ LNO/LFO SLs. a) XAS spectra of Fe and Ni L edges. The spectra of Fe_2O_3 and bulk LNO taken from ref. [43] and ref. [11] are included for reference. b,c) Polarization-dependent XAS spectra around Ni L_2 edge and corresponding linear dichroism (LD) for the SLs grown on STO (b) and Si/STO (c) substrates.

sensitive total electron yield mode (Figure S6, Supporting Information), which yielded consistent results. From the energy shift of Ni L_2 edge, the splitting energy, ΔE is estimated as 56 ± 5 meV for the $n = 4$ SL grown on Si/STO, very close to the corresponding SL epitaxially strained to $DyScO_3$ (DSO) substrate showing $\Delta E \approx 52 \pm 5$ meV (Figure S7, Supporting Information). To further quantify this orbital polarization, the hole ratio r is calculated using the sum rule[8]

$$r = \frac{h_{3z^2-r^2}}{h_{x^2-y^2}} = \frac{3I(c)}{4I(ab) - I(c)} \quad (2)$$

where $h_{3z^2-r^2}$ and $h_{x^2-y^2}$ represent the number of holes in the $3z^2$–r^2 and x^2–y^2 orbitals, respectively. For the SL grown on Si/STO, the hole ratio r is calculated to be ≈1.118, slightly smaller than $r = 1.135$ reported for LNO/DSO SL epitaxially strained to DSO substrate.[9] This is in line with the difference in strain states. The $n = 4$ SL on STO/Si suffers a tensile strain of ≈2.4%, as compared to the epitaxial strain of ≈2.76% imposed by DSO.

The absence of orbital polarization in LNO/LFO SL grown on STO is rather surprising considering the in-plane epitaxial strain of ≈1.7%. This is, however, in agreement with previous observations in LNO/STO single films, where the strain is accommodated by suppressed NiO_6 octahedral rotations along the out-of-plane axis, together with an emergent breathing distortion of NiO_6 octahedra.[11,20,21] The preserved isotropic crystal field hardly influences the orbital configuration of Ni^{3+} ion. In stark contrast with the LNO/LFO SL on STO, we observed a robust Ni x^2–y^2 orbital polarization in LNO/LAO SL under the same amount of strain, albeit without any energy splitting (Figure S8, Supporting Information). It has been argued that the stronger ionicity of Al^{3+}—O^{2-} than Ni^{3+}—O^{2-} bond gives rise to a reduced hole density for apical oxygen at the interface, which reduces the electron occupancy of Ni $3z^2$–r^2 orbital even without crystal field splitting.[10] This scenario can account for the absence of orbital polarization in our LNO/LFO SL grown on STO by considering the small difference in ionicity between Ni^{3+}—O^{2-} and Fe^{3+}—O^{2-} bonds. For the SLs grown on Si/STO and DSO substrates, the larger tensile strain induces a sizable crystal field splitting, as revealed by the energy shift of Ni L_2 edge, and consequent Ni x^2–y^2 orbital polarization.

To summarize, LFO/LNO SLs have been fabricated on STO and Si/STO substrates. The strain states evolve distinctly in the two sets of SLs as a function of the layer thickness of LNO, n. In contrast with the coherently strained state for all n on STO substrates, the in-plane lattice parameter of the SLs on Si/STO is dictated by the SL composition along with the thermal strain from Si, which gradually decays with increasing n. Both sets of SLs show MITs upon reducing n and the onset of strong electron localization occurs at $n = 3$. The substantially larger strain on Si/STO leads to enhanced T_{MI} at $n = 4$ and increased resistivity at $n = 1$, 2, but hardly influences the electron conduction mechanisms at all n. In particular, the large tensile strain promotes a pronounced Ni $3d_{x^2-y^2}$ orbital polarization in the SL grown on Si/STO, comparable to the LNO SLs epitaxially strained to DSO substrate. Our results demonstrate that thermal strain can be exploited to engineer the orbital states in functional oxides, in analogy to the conventional epitaxial strain. It is interesting to note that the amount of strain for oxide films grown on silicon can be further tuned by elevating the deposition temperature,[22] offering new freedoms to design the strain states. Finally, we hope this study can stimulate more research into the exploration of new functionalities in oxide SLs integrated on silicon.

Experimental Section

The PLD growth of LNO/LFO SLs was conducted at 650 °C at an oxygen partial pressure of 0.04 mbar. The laser fluence and frequency were set to 2 J cm^{-2} and 2 Hz, respectively. The samples were in situ annealed for 10 min before cooling down to room temperature. The single terminated and terraced STO substrates were obtained by a chemical etching with buffered hydrofluoric acid and a subsequent annealing in flowing oxygen at 950 °C for 90 min. The surface morphology was characterized using atomic force microscopy. The XRD measurements were conducted on the PANalytical-X'Pert material research diffractometer. The cross-sectional scanning transmission electron microscopy high angle dark field images were acquired on the

© 2020 The Authors. Advanced Materials published by Wiley-VCH GmbH

X-Ant-Em instrument operated at 300 kV. The temperature dependent resistivities were measured with a van der Pauw geometry on a Quantum Design physical property measurement system. The XAS experiments were performed on the XTreme beamline at Swiss Light Source.[45]

Supporting Information

Supporting Information is available from the Wiley Online Library or from the author.

Acknowledgements

This work is supported by the international M-ERA.NET project SIOX (project 4288) and H2020 project ULPEC (project 732642). M.S. acknowledges funding from Slovenian Research Agency (Grants No. J2-9237 and No. P2-0091). This work received support from the ERC CoG MINT (#615759) and from a PHC Van Gogh grant. M.B. thanks the French Academy of Science and the Royal Netherlands Academy of Arts and Sciences for supporting his stays in the Netherlands. This project has received funding as a transnational access project from the European Union's Horizon 2020 research and innovation programme under grant agreement No 823717 - ESTEEM3. N.G. and J.V. acknowledge GOA project "Solarpaint" of the University of Antwerp.

Conflict of Interest

The authors declare no conflict of interest.

Keywords

metal-to-insulator transition, nickelate superlattices, orbital polarization, silicon, strain

Received: July 22, 2020
Revised: September 27, 2020
Published online: November 11, 2020

[1] R. A. Mckee, F. J. Walker, M. F. Chisholm, *Phys. Rev. Lett.* **1998**, *81*, 3014.
[2] S. Middey, J. Chakhalian, P. Mahadevan, J. W. Freeland, A. J. Millis, D. D. Sarma, *Annu. Rev. Mater. Res.* **2016**, *46*, 305.
[3] A. V. Boris, Y. Matiks, E. Benckiser, A. Frano, P. Popovich, V. Hinkov, P. Wochner, M. Castro-Colin, E. Detemple, V. K. Malik, C. Bernhard, T. Prokscha, A. Suter, Z. Salman, E. Morenzoni, G. Cristiani, H.-U. Habermeier, B. Keimer, *Science* **2011**, *332*, 937.
[4] B. Chen, H. Xu, C. Ma, S. Mattauch, D. Lan, F. Jin, Z. Guo, S. Wan, P. Chen, G. Gao, F. Chen, Y. Su, W. Wu, *Science* **2017**, *357*, 191.
[5] J. Chaloupka, G. Khaliullin, *Phys. Rev. Lett.* **2008**, *100*, 016404.
[6] P. Hansmann, X. Yang, A. Toschi, G. Khaliullin, O. K. Andersen, K. Held, *Phys. Rev. Lett.* **2009**, *103*, 016401.
[7] A. S. Disa, F. J. Walker, S. Ismail-Beigi, C. H. Ahn, *APL Mater.* **2015**, *3*, 062303.
[8] E. Benckiser, M. W. Haverkort, S. Brück, E. Goering, S. MacKe, A. Frañó, X. Yang, O. K. Andersen, G. Cristiani, H. U. Habermeier, A. V. Boris, I. Zegkinoglou, P. Wochner, H. J. Kim, V. Hinkov, B. Keimer, *Nat. Mater.* **2011**, *10*, 189.
[9] M. Wu, E. Benckiser, M. W. Haverkort, A. Frano, Y. Lu, U. Nwankwo, S. Brück, P. Audehm, E. Goering, S. Macke, V. Hinkov, P. Wochner, G. Christiani, S. Heinze, G. Logvenov, H. U. Habermeier, B. Keimer, *Phys. Rev. B: Condens. Matter Mater. Phys.* **2013**, *88*, 125124.
[10] J. W. Freeland, J. Liu, M. Kareev, B. Gray, J. W. Kim, P. Ryan, R. Pentcheva, J. Chakhalian, *Europhys. Lett.* **2011**, *96*, 57004.
[11] I. C. Tung, P. V. Balachandran, J. Liu, B. A. Gray, E. A. Karapetrova, J. H. Lee, J. Chakhalian, M. J. Bedzyk, J. M. Rondinelli, J. W. Freeland, *Phys. Rev. B: Condens. Matter Mater. Phys.* **2013**, *88*, 205112.
[12] M. J. Han, X. Wang, C. A. Marianetti, A. J. Millis, *Phys. Rev. Lett.* **2011**, *107*, 206804.
[13] R. Scherwitzl, S. Gariglio, M. Gabay, P. Zubko, M. Gibert, J.-M. Triscone, *Phys. Rev. Lett.* **2011**, *106*, 246403.
[14] E. Sakai, M. Tamamitsu, K. Yoshimatsu, S. Okamoto, K. Horiba, M. Oshima, H. Kumigashira, *Phys. Rev. B: Condens. Matter Mater. Phys.* **2013**, *87*, 075132.
[15] P. D. C. King, H. I. Wei, Y. F. Nie, M. Uchida, C. Adamo, S. Zhu, X. He, I. Božović, D. G. Schlom, K. M. Shen, *Nat. Nanotechnol.* **2014**, *9*, 443.
[16] A. Frano, E. Schierle, M. W. Haverkort, Y. Lu, M. Wu, S. Blanco-Canosa, U. Nwankwo, A. V. Boris, P. Wochner, G. Cristiani, H. U. Habermeier, G. Logvenov, V. Hinkov, E. Benckiser, E. Weschke, B. Keimer, *Phys. Rev. Lett.* **2013**, *111*, 106804.
[17] D. P. Kumah, A. S. Disa, J. H. Ngai, H. Chen, A. Malashevich, J. W. Reiner, S. Ismail-Beigi, F. J. Walker, C. H. Ahn, *Adv. Mater.* **2014**, *26*, 1935.
[18] M. Golalikhani, Q. Lei, R. U. Chandrasena, L. Kasaei, H. Park, J. Bai, P. Orgiani, J. Ciston, G. E. Sterbinsky, D. A. Arena, P. Shafer, E. Arenholz, B. A. Davidson, A. J. Millis, A. X. Gray, X. X. Xi, *Nat. Commun.* **2018**, *9*, 2206.
[19] J. Son, P. Moetakef, J. M. Lebeau, D. Ouellette, L. Balents, S. J. Allen, S. Stemmer, *Appl. Phys. Lett.* **2010**, *96*, 062114.
[20] J. Chakhalian, J. M. Rondinelli, J. Liu, B. A. Gray, M. Kareev, E. J. Moon, N. Prasai, J. L. Cohn, M. Varela, I. C. Tung, M. J. Bedzyk, S. G. Altendorf, F. Strigari, B. Dabrowski, L. H. Tjeng, P. J. Ryan, J. W. Freeland, *Phys. Rev. Lett.* **2011**, *107*, 116805.
[21] S. J. May, J. W. Kim, J. M. Rondinelli, E. Karapetrova, N. A. Spaldin, A. Bhattacharya, P. J. Ryan, *Phys. Rev. B: Condens. Matter Mater. Phys.* **2010**, *82*, 014110.
[22] L. Zhang, Y. Yuan, J. Lapano, M. Brahlek, S. Lei, B. Kabius, V. Gopalan, R. Engel-Herbert, *ACS Nano* **2018**, *12*, 1306.
[23] B. Chen, N. Gauquelin, P. Reith, U. Halisdemir, D. Jannis, M. Spreitzer, M. Huijben, S. Abel, J. Fompeyrine, J. Verbeeck, H. Hilgenkamp, G. Rijnders, G. Koster, *Phys. Rev. Mater.* **2020**, *4*, 024406.
[24] M. Chen, T. Wu, J. Wu, *Appl. Phys. Lett.* **1996**, *68*, 1430.
[25] Q. Zou, H. E. Ruda, B. G. Yacobi, *Appl. Phys. Lett.* **2001**, *78*, 1282.
[26] D. Bao, N. Wakiya, K. Shinozaki, N. Mizutani, X. Yao, *Appl. Phys. Lett.* **2001**, *78*, 3286.
[27] C. Marchiori, M. Sousa, A. Guiller, H. Siegwart, J. P. Locquet, J. Fompeyrine, G. J. Norga, J. W. Seo, *Appl. Phys. Lett.* **2006**, *88*, 072913.
[28] J. E. Kleibeuker, Z. Zhong, H. Nishikawa, J. Gabel, A. Müller, F. Pfaff, M. Sing, K. Held, R. Claessen, G. Koster, G. Rijnders, *Phys. Rev. Lett.* **2014**, *113*, 237402.
[29] S. Y. Smolin, A. K. Choquette, R. G. Wilks, N. Gauquelin, R. Félix, D. Gerlach, S. Ueda, A. L. Krick, J. Verbeeck, M. Bär, J. B. Baxter, S. J. May, *Adv. Mater. Interfaces* **2017**, *4*, 1700183.
[30] A. Scholl, J. Stöhr, J. Lüning, J. W. Seo, J. Fompeyrine, H. Siegwart, J. Locquet, F. Nolting, S. Anders, E. E. Fullerton, M. R. Scheinfein, H. A. Padmore, *Science* **2000**, *287*, 1014.
[31] K. H. L. Zhang, G. Li, S. R. Spurgeon, L. Wang, P. Yan, Z. Wang, M. Gu, T. Varga, M. E. Bowden, Z. Zhu, C. Wang, Y. Du, *ACS Appl. Mater. Interfaces* **2018**, *10*, 17480.
[32] S. Middey, D. Meyers, R. Kumar Patel, X. Liu, M. Kareev, P. Shafer, J. W. Kim, P. J. Ryan, J. Chakhalian, *Appl. Phys. Lett.* **2018**, *113*, 081602.
[33] Z. Wang, B. H. Goodge, D. J. Baek, M. J. Zachman, X. Huang, X. Bai, C. M. Brooks, H. Paik, A. B. Mei, J. D. Brock, J. P. Maria, L. F. Kourkoutis, D. G. Schlom, *Phys. Rev. Mater.* **2019**, *3*, 73403.
[34] Z. Wang, Z. Chen, A. B. Mei, X. Bai, L. F. Kourkoutis, D. A. Muller, D. G. Schlom, *J. Vac. Sci. Technol. A* **2018**, *36*, 021507.
[35] A. Fossdal, M. Menon, I. Wærnhus, K. Wiik, M. A. Einarsrud, T. Grande, *J. Am. Ceram. Soc.* **2004**, *87*, 1952.

© 2020 The Authors. Advanced Materials published by Wiley-VCH GmbH

[36] H. Nagamoto, I. Mochida, K. Kagotani, H. Inoue, A. Negishi, *J. Mater. Res.* **1993**, *8*, 3158.
[37] Š. Masys, V. Jonauskas, *Comput. Mater. Sci.* **2015**, *108*, 153.
[38] B. Chen, P. Chen, H. Xu, F. Jin, Z. Guo, D. Lan, S. Wan, G. Gao, F. Chen, W. Wu, *ACS Appl. Mater. Interfaces* **2016**, *8*, 34924.
[39] S. J. May, T. S. Santos, A. Bhattacharya, *Phys. Rev. B: Condens. Matter Mater. Phys.* **2009**, *79*, 115127.
[40] H. Wei, M. Jenderka, M. Bonholzer, M. Grundmann, M. Lorenz, *Appl. Phys. Lett.* **2015**, *106*, 042103.
[41] J. Liu, S. Okamoto, M. van Veenendaal, M. Kareev, B. Gray, P. Ryan, J. W. Freeland, J. Chakhalian, *Phys. Rev. B* **2011**, *83*, 161102(R).
[42] F. Rivadulla, J. S. Zhou, J. B. Goodenough, *Phys. Rev. B: Condens. Matter Mater. Phys.* **2003**, *67*, 165110.
[43] G. Anjum, R. Kumar, S. Mollah, P. Thakur, S. Gautam, K. H. Chae, *J. Phys. D: Appl. Phys.* **2011**, *44*, 075403.
[44] Z. Liao, E. Skoropata, J. W. Freeland, E. J. Guo, R. Desautels, X. Gao, C. Sohn, A. Rastogi, T. Z. Ward, T. Zou, T. Charlton, M. R. Fitzsimmons, H. N. Lee, *Nat. Commun.* **2019**, *10*, 589.
[45] C. Piamonteze, U. Flechsig, S. Rusponi, J. Dreiser, J. Heidler, M. Schmidt, R. Wetter, M. Calvi, T. Schmidt, H. Pruchova, J. Krempasky, C. Quitmann, H. Brune, F. Nolting, *J. Synchrotron Radiat.* **2012**, *19*, 661.

© 2020 The Authors. Advanced Materials published by Wiley-VCH GmbH